Int J Adv Manuf Technol (2016) 83:145–155
DOI 10.1007/s00170-015-7541-0

ORIGINAL ARTICLE

Stress distributions during the cross-wedge rolling of composite 42CrMo/Q235 laminated shafts

W. F. Peng[1] · J. H. Zhang[1] · G. X. Huang[1] · W. P. Liu[1] · X. D. Shu[1] · J. Zhu[1]

Received: 13 April 2015 / Accepted: 2 July 2015 / Published online: 21 July 2015

Abstract Laminated shafts are often used as alternatives to elemental metal shafts, which are prone to corrosion and wear. However, manufacturing laminated shafts is difficult. In this paper, a laminated shaft production method involving cross-wedge rolling was proposed. The cross-wedge rolling of 42CrMo/Q235 laminated shafts was numerically simulated using ANSYS/LS-DYNA software. The deformation characteristics and stress distribution laws of the 42CrMo/Q235 laminated shafts in the knifing zone and stretching zones were obtained. The formation mechanisms of the stress distributions were analyzed, and the theoretical significance of the interface bonding on the cross-wedge-rolled 42CrMo/Q235 laminated shafts was discussed. Furthermore, the feasibility of 42CrMo/Q235 laminated shaft production via cross-wedge rolling was validated. Theoretical foundations were also provided for use in future studies concerning the rolling lamination mechanisms of dissimilar-metal laminated shafts.

Keywords Cross-wedge rolling · Laminated shaft · 42CrMo/Q235 · Stress analysis

✉ X. D. Shu
shuxuedao@nbu.edu.cn

W. F. Peng
pengwenfei@nbu.edu.cn

[1] Zhejiang Provincial Key Lab of Part Rolling Technology, Faculty of Mechanical Engineering and Mechanics, Ningbo University, Ningbo 315211, Peoples' Republic of China

1 Introduction

The development of structural materials with long service lives in supernormal environments has been a topic of numerous studies, with energy, aerospace, steel manufacturing, and chemical engineering applications. However, many of these materials are difficult to manufacture due to numerous complications, such as difficulties maintaining an optimal balance between strengthening and toughening and controlling shape and performance. In addition, since many shafts function in extreme environments with high temperatures, high amount of pressure, and failure issues, such as creep, fatigue, wear, corrosion, and fractures, occur frequently [1–3]. Some conventional solutions used to improve the safety and service lives of shafts have included the use of high-quality precious metals with resistance to high temperatures, corrosion, and wear, and the development of new materials with special characteristics, such as super-strength steel, superalloys, stainless steel, titanium alloys, or rare metals [4, 5]. However, these methods significantly increase manufacturing costs and waste high-quality metals [6]. Therefore, in this paper, a method for manufacturing laminated shafts, which would fully utilize available materials and consist of metal layers with individualized functional roles, was proposed. This method could not only be used to develop new shaft designs but could also be applied to the manufacturing processes of other components used in complex environments.

Lamination and shape formation processes limit the widespread application of laminated shafts. Yahiro et al. [7] used warm rolling to produce non-ferrous metal laminated plates and analyzed the effects of rolling temperature on the qualities of those plates. Lee et al. [8] studied the effects of annealing treatments on the interface microstructures and mechanical performances of rolled STS-Al-Mg laminated plates. Xie et al. [9] conducted both numerical simulations and

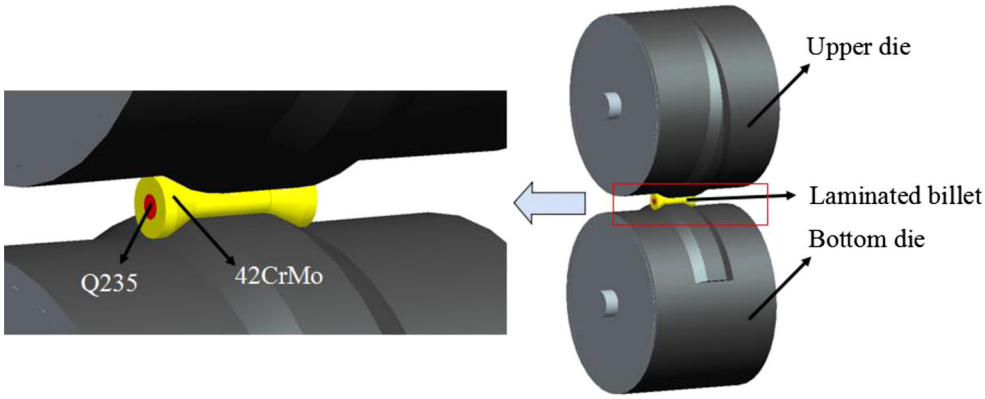

Fig. 1 Schematic diagram of the two-roll cross-wedge rolling process

experimental studies on the metal flow behaviors of copper-clad aluminum laminated bars produced via cold flat rolling, obtaining flat plates with uniformly distributed copper-clad layers and favorable surface qualities. Wang et al. [10] investigated the rolling welding processes and interface-bonding mechanisms of titanium/copper laminated bars. According to these studies, rolling lamination has primarily been used to weld simple rectangular or circular sections. Rolling lamination is highly efficient and yields stable interface qualities. However, step shafts cannot be directly produced by rolling laminated plates, bars, or tubes. Furthermore, cutting processes disproportionately reduce part performance, resulting in wasted materials and decreased production efficiency.

In recent years, cross-wedge rolling studies have only concerned single-layered shafts comprised of 45 steel, 40 Cr, and aluminum alloys [11–22]. For example, Hu et al. [23, 24] investigated GH 4169 super-alloy shaft parts and used 4Cr9Si2 to produce engine valves. Hu found that the surfaces and core areas of cross-wedge-rolled alloy shafts were prone to microcracks and cavities. In addition, Du et al. [25] conducted a systematic theoretical study on the forming behaviors, microstructure performance, and controlled rolling and cooling processes of cross-wedge-rolled, microalloyed, non-quenched, tempered 40MnV steel shafts. Furthermore, Silva et al. [26] studied the damage mechanisms of the centers of cross-wedge-rolled 38MnSiVS5 shafts. In these studies, multi-metal laminated shafts were neglected, and the cross-wedge rolling of dual-metal laminated composite shafts yielded technological complexities and difficulties.

In this paper, the cross-wedge rolling method was used to produce laminated shafts in order to simultaneously prepare, form, and stabilize the interface-bonding performance of composite materials. Finite element models of the dual-metal laminated shafts during cross-wedge rolling were constructed. The stress distributions of the cross-wedge-rolled 42CrMo/Q235 laminated shafts were analyzed in order to reveal the welding mechanisms of the dual-metal laminated shafts. Rolling experiments were also conducted in order to validate the feasibility of 42CrMo/Q235 laminated shaft production via cross-wedge rolling. Furthermore, a method of reducing the weight and extending the service lives of shafts was proposed, and theoretical guidance regarding the cross-wedge rolling of dissimilar-metal laminated shafts was provided.

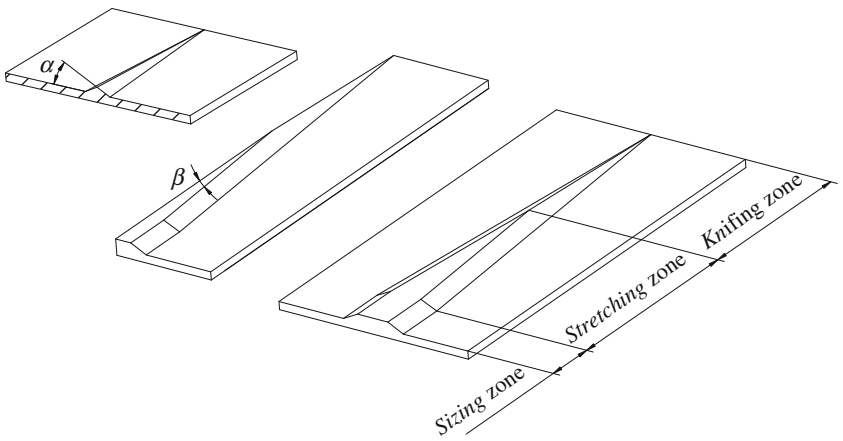

Fig. 2 Geometry of the cross-wedge rolling die, including the forming angle (α), spreading angle (β), and three forming stages

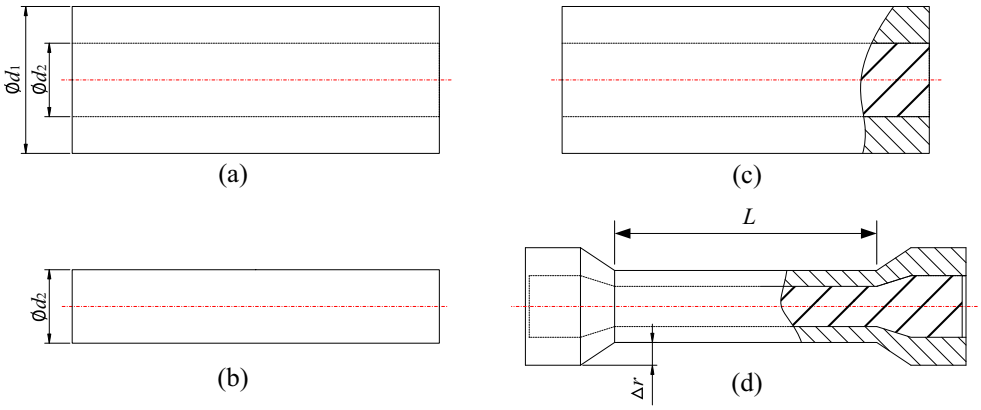

Fig. 3 Geometry of the billet and rolled part. **a** 42CrMo hollow pipe, **b** Q235 bar, **c** assembly of the two materials, and **d** the rolled part

2 The principle of the cross-wedge rolling of laminated shaft

A schematic diagram of the cross-wedge rolling mechanisms of laminated shafts is shown in Fig. 1. In cross-wedge rolling, two wedge-shaped dies rotate in the same direction, causing the composite laminated billet to rotate in the opposite direction [27]. The surface of the un-welded metal can be broken, thereby exposing the activated surface, by applying a high rolling pressure or temperature. The laminated interfaces are metallurgically bonded through the diffusion of atoms, resulting in the production of laminated shafts. The cross-wedge rolling process consists of three stages, including the knifing, stretching, and sizing zones. After the process parameters, such as the forming angle (α), stretching angle (β), and reduction ratio of the cross-sectional area reduction (area reduction ψ), were defined, the cross-wedge rolling die was designed, as shown in Fig. 2. Next, the billet was formed, as shown in Fig. 3. During conventional flat rolling, a nearly uniform distribution of contact stress exists between the two laminated metals, and rolling welding can be performed relatively easily. However, since wedge-shaped dies are used during cross-wedge rolling, the distribution of stress within the contact interface area is not uniform, and rolling welding is difficult to realize.

In order to ensure normal laminated billet rotation, the appropriate process parameters must be implemented [28]. The selected rotation conditions are shown in Eq. 1.

$$\tan\alpha\tan\beta \le \frac{md\mu^2}{\pi d_k\left(1+\frac{d}{D}\right)} \tag{1}$$

α forming angle
β spreading angle
m model number
D mold diameter
d billet diameter
d_k rotation diameter
μ friction coefficient

The forming angle (α), which usually ranges from 20° to 35°, is limited by the porosity of the center and the tensile necking of a laminated billet. The stretching angle (β), according to the limitations of the rotation conditions, can be expressed as follows:

$$\beta \le \tan^{-1}\left[\frac{m\mu^2}{\pi(d_1+\Delta r)\left(\frac{1}{d}+\frac{1}{D}\right)tan\alpha}\right] \tag{2}$$

$$\Delta r = \frac{d-d_1}{2} \tag{3}$$

$$\psi = 1-\left(\frac{d_1}{d}\right)^2 = 1-\left(1-\frac{2\Delta r}{d}\right)^2 \tag{4}$$

d_1 shaft diameter
Δr total amount of compression

3 Finite element model and experiment

The finite element model of a cross-wedge rolling laminated shaft must be obtained before analyzing its stress distribution laws. Experiments concerning the practicality of cross-wedge-rolling welding were also conducted in this study.

Table 1 Regression coefficients of the 42CrMo and Q235 deformation resistance models

Steel	σ_0 (MPa)	a_1	a_2	a_3	a_4	a_5	a_6
42CrMo	153.0	−2.982	3.796	0.2508	−0.1810	0.4160	1.483
Q235	150.6	−2.878	3.665	0.1861	−0.1216	0.3795	1.402

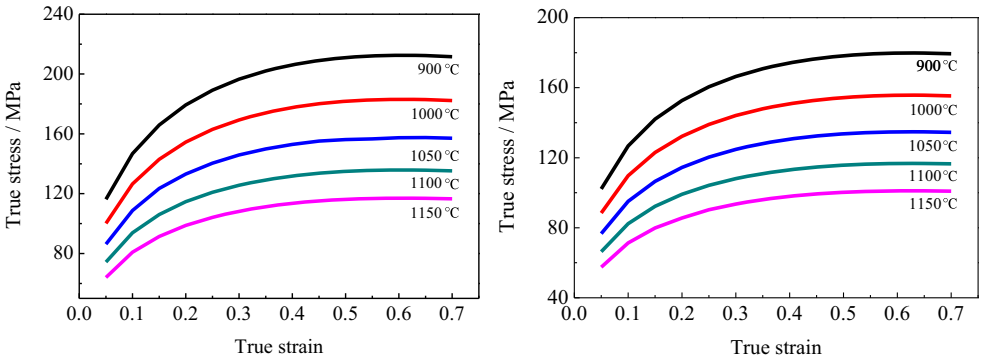

Fig. 4 Stress-strain curves of the **a** 42CrMo and **b** Q235

3.1 Material properties

The forming temperature of a metal significantly influences its plastic deformation resistance. Thus, mathematical models of the materials under various temperatures, strain rates, and amounts of deformation were obtained in order to determine the accurate forming mechanisms of the cross-wedge-rolled laminated shafts. In this paper, the plastic deformation resistance model shown in Eq. 3 was adopted [29].

$$\sigma = \sigma_0 exp(\alpha_1 T + \alpha_2)\left(\frac{u}{10}\right)^{\alpha_3 T+\alpha_4}\left[\alpha_6\left(\frac{\gamma}{0.4}\right)^{\alpha_5} - (\alpha_6 - 1)\frac{\gamma}{0.4}\right] \quad (5)$$

where $T = \frac{t+273}{1000}$

σ_0	basic deformation resistance, when T=1000 °C, γ=0.4, and u=10 s^{-1}
T	deformation temperature (°C)
u	deformation rate (s^{-1})
γ	degree of deformation
σ_0, a_1~a_6	regression coefficients, the values of which depend on the steel material

The regression coefficients of the 42CrMo and Q235 deformation resistance models are listed in Table 1. The clad material used in this study was 42CrMo. The stress-strain curve of this material is displayed in Fig. 4a. The core material used in this study was Q235. The stress-strain curve of this material is displayed in Fig. 4b.

3.2 Geometric and process parameters

The process parameters, such as the forming angle (α), stretching angle (β), and area of reduction (Ψ), and geometric parameters of the laminated billet and dies are displayed in Table 2.

3.3 Boundary conditions

The cross-wedge rolling of composite laminated shafts entails not only radial compression, axial tensile, and lateral stretching but also interactions among the interfaces of the composite materials. Both material nonlinearity (nonlinearity between stress and strain) and geometric nonlinearity (nonlinearity between strain and displacement), which have complex boundary conditions, are present during the cross-wedge rolling process. When constructing a finite element model, a minimum of seven factors must be considered in order to obtain an accurate description of the forming process. Thus, in this study, the following assumptions were implemented:

1. Since the rolling process was conducted at 1050 °C, the elastic deformation of the dies was assumed to be much less than that of the laminated billet. Hence, elastic die deformation was neglected. By assuming that the dies were rigid bodies, the number of computations was largely reduced. Rigid shell elements (shell 63) with an elastic modulus (E) of 210 GPa were used to mesh the dies.
2. The self-weights of both the clad and core materials were negated, and both of these materials were assumed to be elastic-plastic bodies. An eight-node 3D solid element (solid 164) was used for meshing. The two layers did not separate during rolling. The elastic modulus (E) of the laminated billet material was 90 GPa.

Table 2 Technological parameters of the cross-wedge-rolled laminated shaft

Process parameters	Value
Forming angel, α/°	28
Spreading angel, β/°	7
Area reduction, ψ/%	60
Die diameter, D/mm	630
Clad material diameter, d_1/mm	40
Core material diameter, d_2/mm	24
Length of the billet, L/mm	100
Temperature, T/°C	1050

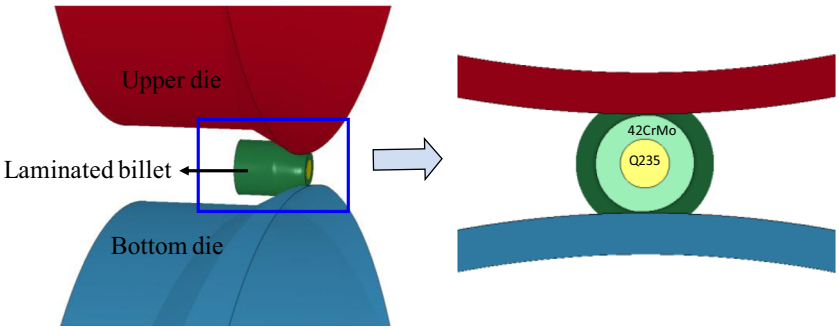

Fig. 5 Finite element model of the cross-wedge-rolled laminated shaft

3. A surface-to-surface contact model (STS) was used for the dies and laminated billet. The die surfaces (rigid bodies) were considered the target surfaces, while the laminated billet surfaces (deformation bodies) were considered the contact surfaces.
4. The rolling process was completed within a very short amount of time, and the time available for heat transfer between the dies and air was limited. Thus, the laminated billet was assumed to be adiabatic during rolling.
5. The friction between the dies and the laminated billet was simplified as Coulomb friction, and the frictional coefficients of all of the areas of contact between the dies and the laminated billet were assumed to be equal (μ=0.50).
6. The laminated billet was assumed to have no contact with the guide plate during rolling; thus, the rolling conditions of the laminated billet and two dies were assumed to be completely symmetrical.

Based on the laws of symmetry, only half of the dies and laminated billet were computed; axial geometrical constraints were applied to the symmetrical surface.

The finite element model of the cross-wedge rolling of the dual-layer-metal laminated shaft constructed using the ANSYS/LS DNA software is shown in Fig. 5. The finite element simulation of the rolling process of the laminated shaft is illustrated in Fig. 6.

3.4 Experiment

Rolling experiments were designed in order to investigate the applicability of cross-wedge rolling to laminated shafts. Process parameters, such as the forming angle (α), stretching angle (β), and area of reduction (Ψ), and geometric parameters of the laminated billet and dies are displayed in Table 3.

An H630 rolling mill was used to conduct the rolling experiments, as shown in Fig. 7b. As shown in Fig. 7a, the laminated billet was assembled from a clad-material open tube

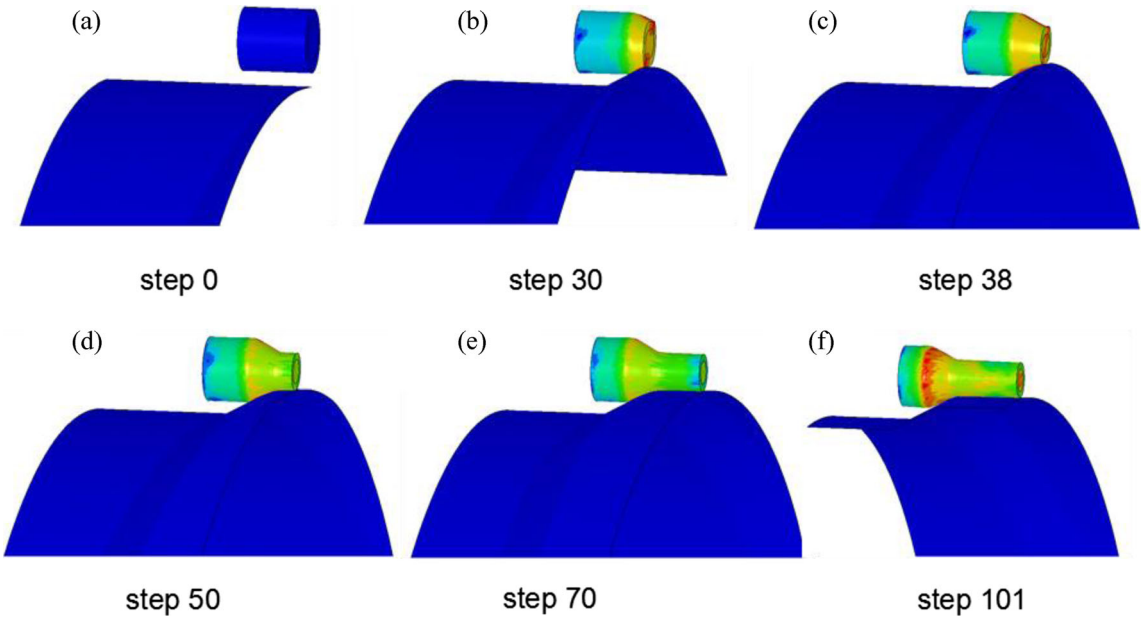

Fig. 6 Finite element simulation of the laminated shaft during the rolling process. **a** Step 0, **b** step 30, **c** step 38, **d** step 50, **e** step 70, and **f** step 101

Table 3 Experimental parameters

Item	Forming angle α (°)	Stretching angle β (°)	Area reduction Ψ (%)	Clad material diameter d_1 (mm)	Core material diameter d_2 (mm)
1	27	5	45	40	20
2	27	5	45	40	22
3	27	3	55	40	22
4	27	5	45	40	24
5	27	3	45	40	24

and core-material solid bar. The surfaces of the clad-material open tube and core-material solid bar were cleaned before assembly. The rolled parts were constructed through the cross-wedge rolling process shown in Fig. 7c according to the experimental parameters in Table 3. As shown in Fig. 7c, some defects, such as non-welded areas, cracks, and holes, were apparent. Some good rolled parts, in which the clad-material open tube was welded to the core-material solid bar, were also obtained. The factors that affected the quality of the rolled parts were analyzed based on their stress distributions.

4 Results and discussion

The cross-wedge rolling process consists of knifing, stretching, and sizing zones. The knifing and stretching zones are the two main deformation stages. In order to reveal the stress distribution laws, an analysis was conducted on the stress fields of these two stages.

4.1 Knifing zone stress analysis

4.1.1 Cross-sectional stress analysis

Figure 8a displays the lateral stress (σ_x) distribution diagram. A relatively large amount of compressive stress was produced in the clad material just below the die contact area. As the distance from the contact point increased, the amount of pressure decreased. Since the dies caused the laminated billet to rotate counterclockwise, the metal flowed toward the exit. Thus, lateral compressive stress was generated in the surface entrance (point A) of the clad material. The lateral stress, which ranged from −57.72 to −22.12 MPa, did not penetrate the core material. The lateral deformation of the clad material comprised the majority of the laminated billet deformation.

Figure 8b displays the radial stress (σ_y) distribution diagram. As shown in this figure, a relatively high amount of compressive stress occurred in a localized area of the laminated billet just beneath the contact area. The compressive stress decreased as the distance from the contact area increased. The

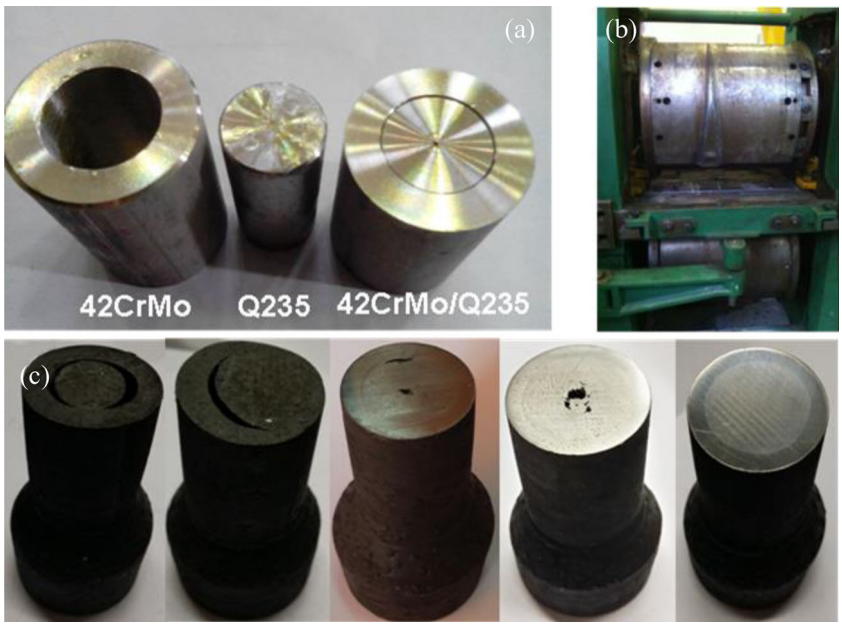

Fig. 7 Experimental rolling process. **a** Assembly of the clad and core materials, **b** cross-wedge rolling mill, and **c** laminated shaft

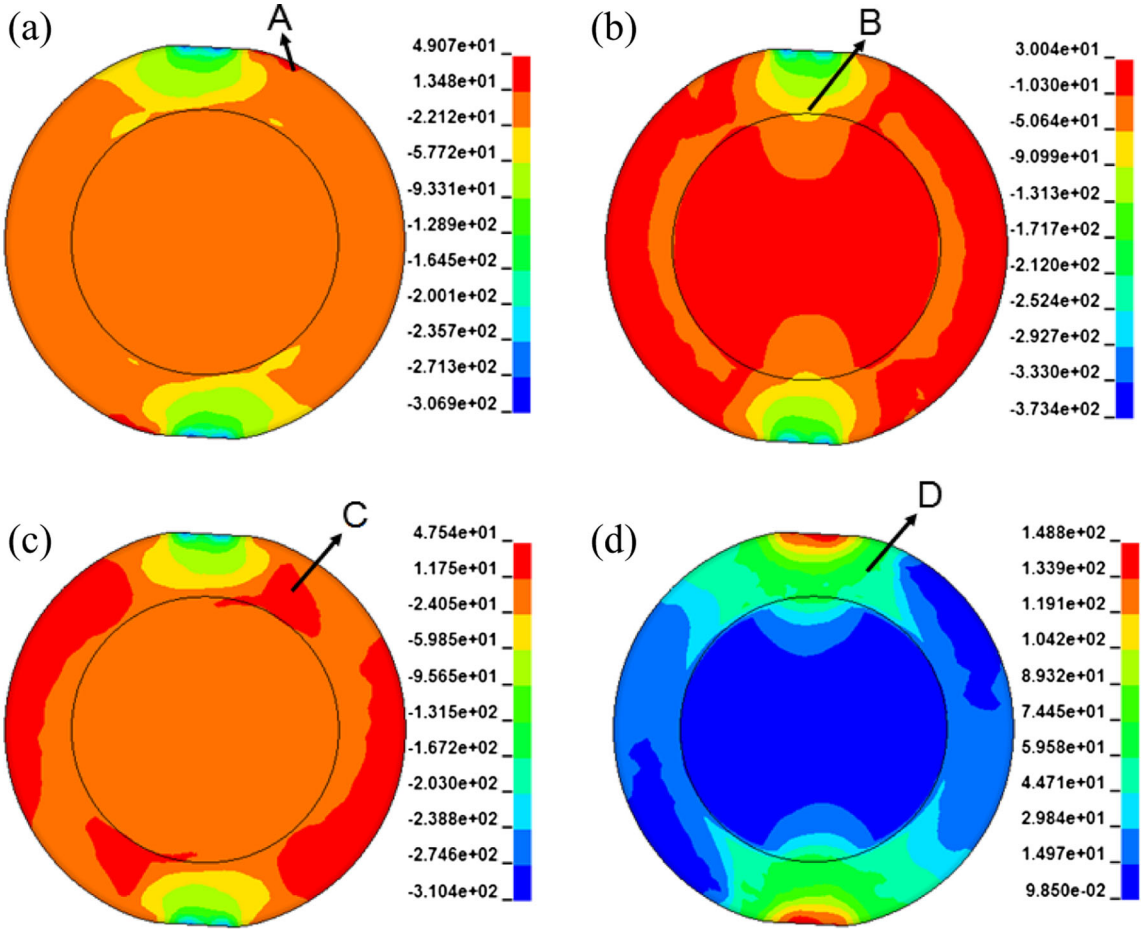

Fig. 8 Cross-sectional stress distribution of the 42CrMo/Q235 laminated shaft in the stretching zone. **a** Lateral stress, **b** radial stress, **c** axial stress, and **d** equivalent stress

compressive stress was still distinct in the surface of the core material. The radial compressive stress ranged from −90.99 to −50.64 MPa. Radial compressive stress also occurred in the core material just below the die. As shown in zone B in this figure, the compressive stress penetrated the core material. The compressive stress penetrated the core material more than the other stress, indicating that compressive stress was the primary type of stress during billet lamination.

Figure 8c displays the axial stress (σ_z) distribution diagram. The stress between the laminated billet and die consisted of compressive stress. As the distance from the contact point increased, the amount of stress decreased. The axial compressive stress decreased to zero before reaching the surface of the core material. In addition, the tensile stress primarily influenced the other gross areas of the clad material. The tensile stress was distributed at the entrance near the internal sidewall of the clad material, partially penetrating the core material. Since the dies caused the laminated billet to rotate counterclockwise, and the pressure and frictional forces applied to the core by the clad material were adequate at point C, this phenomenon was attributed to the axial stretching of the core material, resulting in axial tensile stress.

Figure 8d displays the equivalent stress distribution diagram. The equivalent stress was primarily distributed within the clad material; the highest levels of equivalent stress were located in the area of contact between the clad material and dies. In the sizing zone, the stress within the core primarily consisted of radial compressive stress generated by radial compression. The clad material did not significantly influence the amounts of lateral or axial stress.

4.1.2 Longitudinal stress analysis

Figure 9a illustrates the lateral stress (σ_x) distribution diagram. As shown in this figure, the lateral compressive stress was concentrated in the areas of contact with the dies. The lateral compressive stress within the interface ranged from approximately −59.85 to −100.1 MPa. Lateral compressive stress was also generated in a localized area within the core. Lateral tensile stress occurred in zone A of the clad material. This was attributed to the compressive deformation and eventual

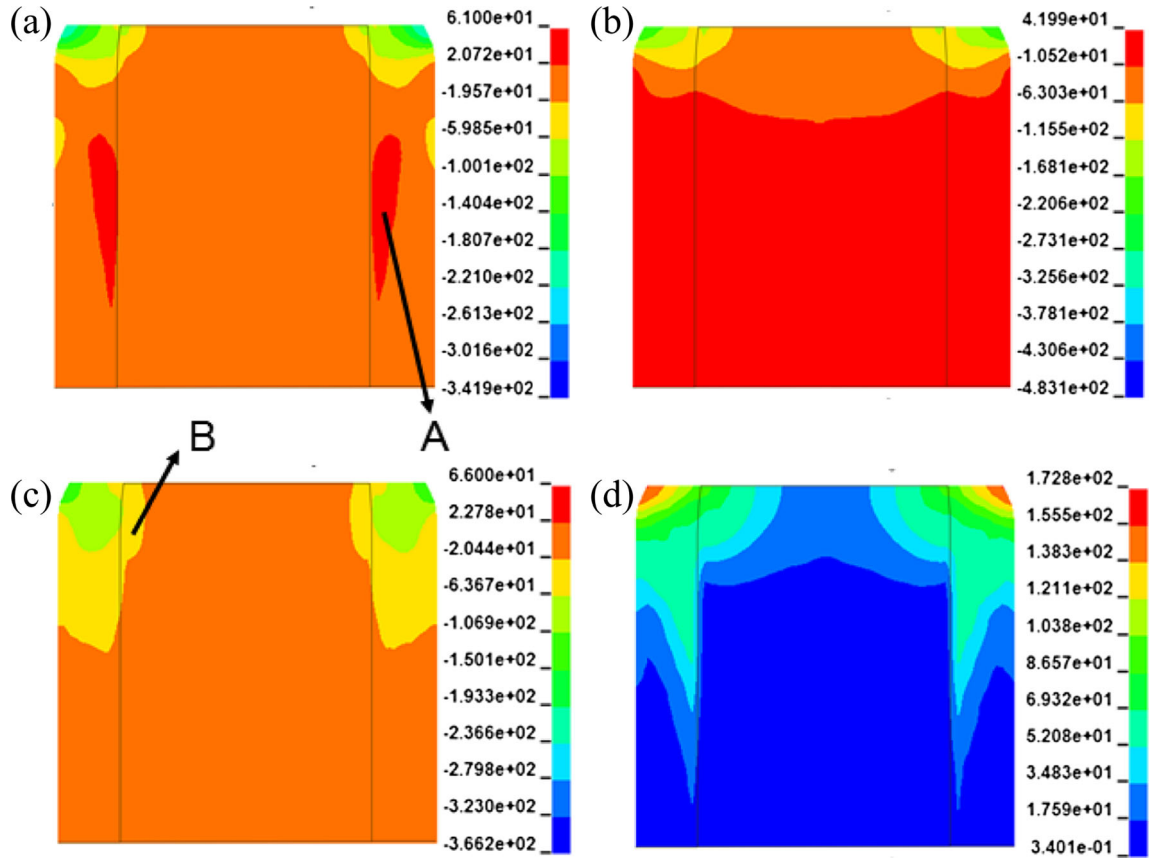

Fig. 9 Longitudinal stress distributions of the 42CrMo/Q235 laminated shaft in the stretching zone. **a** Lateral stress distribution, **b** radial stress distribution, **c** axial stress distribution, and **d** equivalent stress distribution

lateral ovalization of the clad material, which caused the metal outside of the rolling zone to stretch. If appropriate process parameters had not been properly selected, the clad material would have exhibited large amounts of lateral deformation, increasing the likelihood of separation between the clad and core materials outside of the rolling zone.

Figure 9b displays the radial stress (σ_y) distribution diagram. The compressive stress was primarily concentrated just below the die contact point. The compressive stress was widely distributed within the core. The lateral compressive stress in the interface within the core ranged from approximately −155.5 to −168.1 MPa.

Figure 9c displays the axial stress (σ_z) distribution diagram. Axial compressive stress was generated in the outer layer of the clad material. A small amount of axial compressive stress was also produced in zone B just below the die due to the weak influence of the clad material on the core material in the sizing zone.

Figure 9d displays the equivalent stress distribution diagram. Beneath the dies, the equivalent stress gradually penetrated the core from the clad material. However, outside of the rolling zone, the equivalent stress was concentrated within the clad material. Faults occurred in the interface. Due to the effects of the lateral and axial compressive stress on the clad material, the equivalent stress in the clad material was distributed along the interface. The sizing zone deformation occurred primarily in the clad material.

4.2 Stretching zone stress analysis

4.2.1 Cross-sectional stress analysis

Figure 10a displays the lateral stress (σ_x) distribution diagram. In the areas of contact with the die, lateral stress was produced in the laminated billet and penetrated the core material. In the interface, the maximum compressive stress ranged from −129.4 to 183.3 MPa. The stress values of the clad and core materials within the interface were similar. After the clad material was welded to the core material through rolling, the lateral flow of the metal induced lateral tensile stress within the core of the core material (A). Tensile stress also occurred at the exit of the clad material, indicating that the clad material exhibited an ovalization tendency.

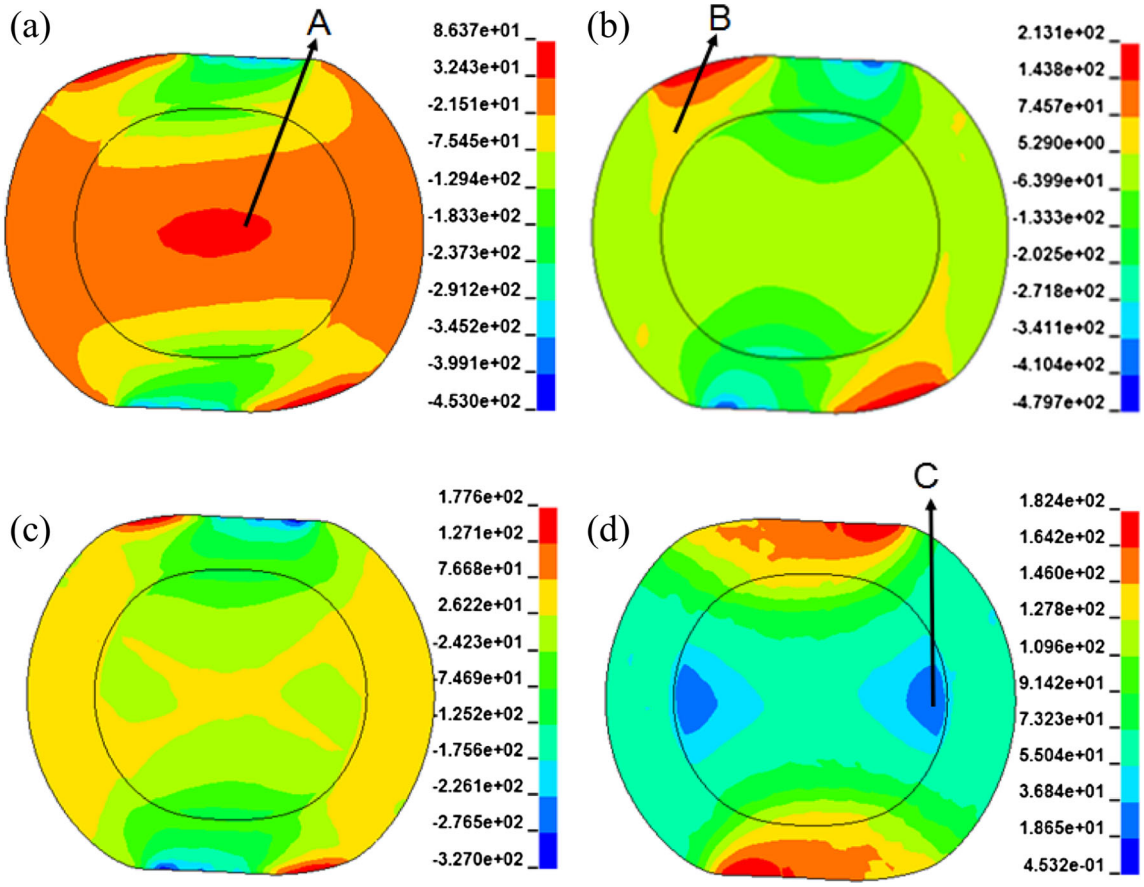

Fig. 10 Cross-sectional stress distributions of the 42CrMo/Q235 laminated shaft in the stretching zone. **a** Lateral stress distribution, **b** radial stress distribution, **c** axial stress distribution, and **d** equivalent stress distribution

Figure 10b displays the radial stress (σ_y) distribution diagram. Large amounts of radial compressive stress were generated at the interface between the clad and core materials just below the areas of contact with the die. The compressive stress values ranged from approximately −202.5 to −271.8 MPa. The stress values of the clad and core materials were similar. The radial necking of the nearby metal introduced radial tensile stress in the exit (B). Point B exhibited a relatively low amount of tensile stress (5.29 MPa) near the core.

Figure 10c displays the axial stress (σ_z) distribution diagram. Just below the areas of contact with the die, both the clad and core materials were compressed as the other areas stretched.

Figure 10d displays the equivalent stress distribution diagram. As the distance from the center, the area of contact with the die in the rolling zone of the laminated billet, decreased, the equivalent stress also decreased. In the interface, the equivalent stress steadily expanded to the core. However, the amount of equivalent stress in area C at either side of the core was relatively low. This was attributed to the low levels of compressive stress in the axial direction of area C. In general, the stress values were similar.

4.2.2 Longitudinal stress analysis

Figure 11a displays the lateral stress (σ_x) distribution diagram. The amount of lateral stress decreased gradually from the outer surface to the core. The center of the core exhibited tensile stress. Between the formed and forming areas, the stress between the clad and core materials transitioned steadily without any faults. However, the transition of stress in the unrolled area was more delayed in the core material than in the clad material. The amount of lateral stress varied significantly at both ends and less in the middle.

Figure 11b displays the radial stress (σ_y) distribution diagram. The radial stress transitioned steadily from the outer layer to the core without faults.

Figure 11c displays the axial stress (σ_z) distribution diagram. The stress transitioned steadily in the rolling zone, with a maximum value in the area of contact with the die.

Figure 11d displays the equivalent stress distribution diagram. As shown in this figure, the amount of equivalent stress was highest in the forming zone, ranging from 144.8 to 163.5 MPa throughout the entire cross section. In the formed zone, the equivalent stress was uniform, indicating that the

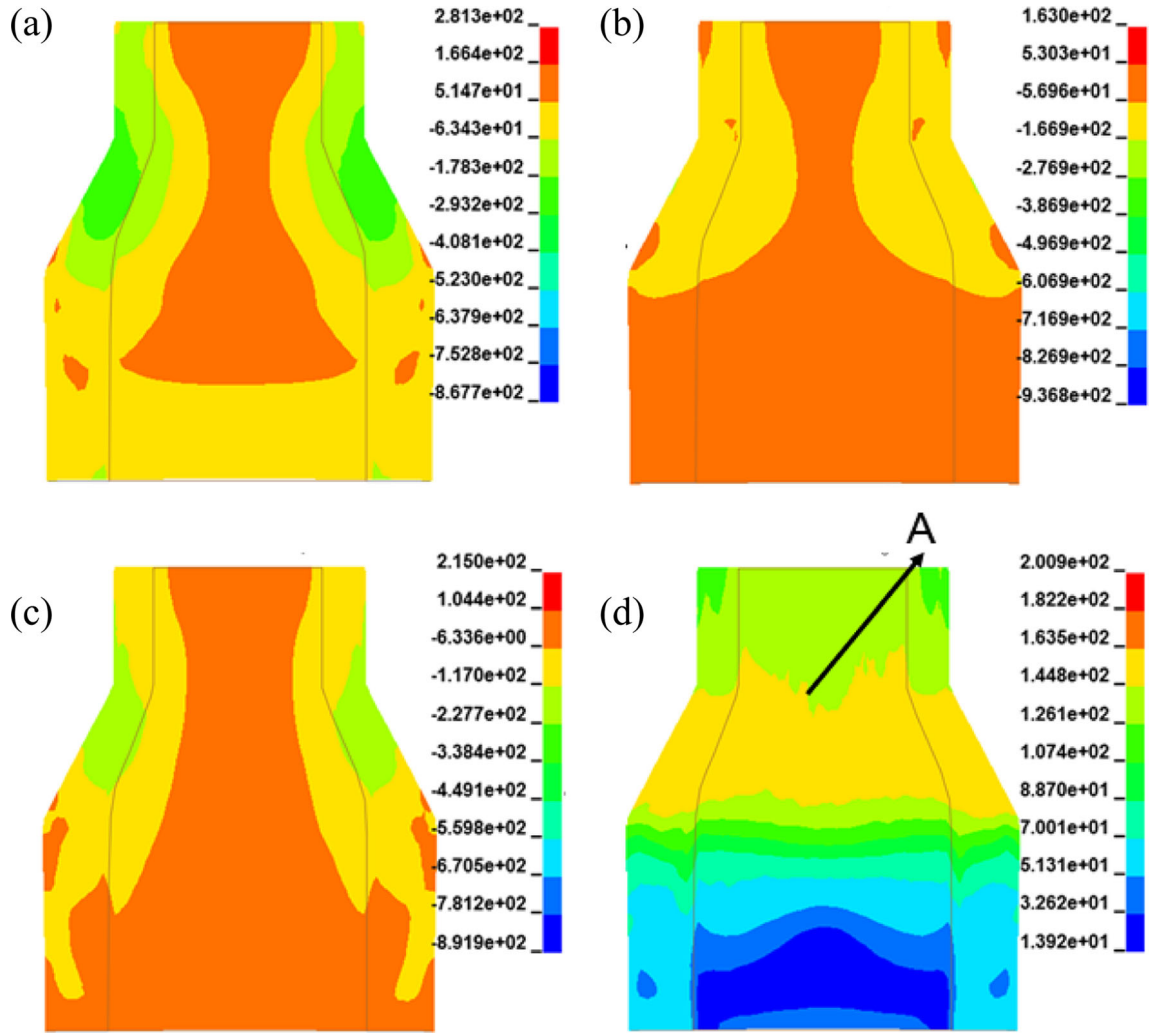

Fig. 11 Longitudinal stress distributions of the 42CrMo/Q235 laminated shaft in the stretching zone. **a** Lateral stress distribution, **b** radial stress distribution, **c** axial stress distribution, and **d** equivalent stress distribution

two layers were bound well, particularly near the interface. No stress concentrations or faults were apparent. Since a large portion of the un-rolled area in the clad material was subjected to axial stress, more equivalent stress was present in the un-formed area of the clad material than that of the core material, no interfaces were apparent. Thus, the stress values were significantly different, and the interface was not welded.

5 Conclusions

1. In the knifing zone, compressive stress primarily occurred just below the die in the clad material. A limited amount of compressive stress penetrated the core, and little core deformation occurred. The amount of equivalent stress between the clad and core materials in the interface was relatively high, indicating that the interface of the sizing zone was difficult to weld. Tensile stress was present in the un-rolled area of the clad material near the interface. If appropriate process parameters had not been properly selected, the clad material would have exhibited large amounts of lateral deformation, increasing the likelihood of separation between the clad and core materials outside of the rolling zone.
2. In the stretching zone, the stress penetrated the core, resulting in significant deformation. The stress values of the clad and core materials in the interface were not significantly different. The stress transitioned from the clad and core materials steadily, indicating that the stretching zone was the primary stage of interface welding.
3. Radial stress, followed by lateral stress, contributed the most to interface welding. Axial stress contributed the least to interface welding.
4. 42CrMo/Q235 laminated shaft could be produced via CWR.

Acknowledgments This project was supported by the National Natural Science Foundation of China (Grant No. 51405248 and 51475247), the International Science and Technology Cooperation Projects (Grant No. CB11-13), the Natural Science Foundation of Ningbo City (Grant No. 2013A610043), and the K.C. Wong Magna Fund in Ningbo University.

References

1. Liu S, Yue ZW, Ma CH (2011) Fracture analysis on the input shaft of coal pulverize reducer of 350 MW supercritical unit. Phys Exam Test 29(5):36–39 **(in Chinese)**
2. Rojo I, Psarra A, Pachidis V, Pilidis P (2010) Evaluation of the energy dissipated as friction/heat between turbines following shaft failure. Proceedings of the ASME Turbo Expo (6): 1345–1352 (in Chinese)
3. Zhang XY, Fu CA, Huang QS (2009) Losing efficiency analysis and improved design of broken shaft of vibration reducer on a certain aircraft. Aircr Des 29(5):28–31 **(in Chinese)**
4. Cassada W, Liu J, Staley J (2002) Aluminum alloys for aircraft structures. Adv Mater Process 160(12):27–29
5. Jiang Y, Yin ZD, Zhu JC, Li MW (2004) Development of ultra-high strength maraging steel. Special Steel 25(2):1–5 **(in Chinese)**
6. Chen YX, Liang XB, Shuang JC, Xu BS (2013) Analysis of FEA of residual stress for thermal sprayed coating on shaft parts. Trans Chin Weld Institut 34(6):13–16
7. Yahiro A, Masui T, Yoshida T, Doi D (1991) Development of non-ferrous clad plate and sheet by warm rolling with different temperature of materials. ISIJ Int 31(6):647–654
8. Seok LK, Hyun YD, Kyoung KH (2012) Effect of annealing on the interface microstructure and mechanical properties of a STS-Al-Mg 3-ply clad sheet. Mater Sci Eng A 556:319–330
9. Luo YB, Liu XH, Xie JX (2009) Lateral spreading deformation behavior in flat rolling of copper cladding aluminum composite rods. Chin J Nonferrous Metal 19(11):1976–1981
10. Li DJ, Wang HK, Yi Z (2004) Heating effect on bonding strength of Ti/Cu cladding bar by pass rolling. Met Form Technol 22(1):46–48 **(in Chinese)**
11. Zbigniew P, Andrzej G, Arkadiusz T (2011) Analysis of the cross-wedge rolling process of toothed shafts made from 2618 aluminium alloy. J Shanghai Jiaotong Univ 16(2):162–166
12. Bartnicki J, Pater Z (2005) Numerical simulation of three-rolls cross wedge rolling of hollowed shaft. J Mater Process Technol 164–165: 1154–1159
13. Pater Z (2006) Finite element analysis of cross wedge rolling. J Mater Process Technol 173:201–208
14. Pater Z (2000) Theoretical and experiment analysis of cross wedge rolling process. Int J Mach Tools Manuf 40:49–60
15. Pater Z (1999) Numerical simulation of the cross wedge rolling process including upsetting. J Mater Process Technol 92–93:468–473
16. Peng WF, Zhang KS, Jia Z, Hu ZH (2010) Analysis on finite element model of cross wedge rolling asymmetric shaft-parts. J Plastic Eng 17(2):79–83 **(in Chinese)**
17. Matveev AV, Safonov AS, Medvedev VE (2002) Modern equipment and technology of billets cross-wedge rolling of machine-building components. Tyazheloe Mashinostroenie 5:12–15
18. Li Q, Lovell MR (2008) Cross wedge rolling failure mechanism and industrial application. Int J Adv Manuf Technol 37:265–278
19. Li Q, Lovell MR (2002) Predicting critical friction in a two-roll cross wedge rolling process. J Tribol 125:200–203
20. Li Q, Lovell MR (2004) The establishment of a failure criterion in cross wedge rolling. Int J Adv Manuf Technol 24:180–189
21. Li Q, Lovell MR (2005) On the critical interfacial friction of a two roll CWR process. J Mater Process Technol 160:245–256
22. Zhou J, Chuan X, Ying YY, Jia Z (2013) Influence of tool parameters on tool wear in two-roll cross-wedge roll. Int J Adv Manuf Technol 65:745–753
23. Zhang N, Wang BY, Hu ZH (2011) Thermomechanical coupled numerical simulation of GH4169 alloy for cross wedge rolling. J Univ Sci Technol Beijing 33(11):1396–1401
24. Ji HC, Liu JP, Wang BY, Zheng ZH, Huang JH, Hu ZH (2015) Cross-wedge rolling of a 4Cr9Si2 hollow valve: explorative experiment and finite element simulation. Int J Adv Manuf Technol 77: 15–26
25. Wang MT, Li XT, Du FS (2005) A coupled thermal–mechanical and microstructural simulation of the cross wedge rolling process and experimental verification. Mater Sci Eng A 391:305–312
26. Silva MLN, Pires GH, Button ST (2011) Damage evolution during cross wedge rolling of steel DIN 38MnSiVS5. 11th Int Conf Mech Behav Mat 10:752–757
27. Shu Xuedao, Valery Ya.Shchukin, G.Kozhevnikova, Sun Baoshou, Peng Wenfei (2014) The theory and forming technology of cross wedge rolling. Publ House Science Beijing
28. Hu ZH, Zhang KS, Wang BY, Shu XD (2004) Formed technology and simulation of parts about the cross-wedge rolling. Publ House Metall Ind Beijing
29. Zhou JH, Guan KZ, Liu J, Liu WH (1991) An mathematical model of flow stress for hot strip mill. J Univ Sci Technol Beijing 13(1): 20–25